RF Information Harvesting for Medium Access in Event-driven Batteryless Sensing

N. H. Hokke[1*], S. Sharma[2], R.V. Prasad[2], L. Mottola[3], S. Narayana[2], V. Rao[4], N. Kouvelas[2]
[1]Zero Energy Development B.V., [2]Delft University of Technology, [3]Politecnico di Milano, [4]Cognizant

ABSTRACT

We present *radio-frequency (RF) information harvesting*, a channel sensing technique that takes advantage of the energy in the wireless medium to detect channel activity at essentially no energy cost. RF information harvesting is essential for event-driven energy harvesting wireless sensing applications using batteryless devices that harvest tiny amounts of energy from impromptu events, such as operating a switch, and then transmit the event notification to a one-hop gateway. As multiple such devices may concurrently detect events, coordinating access to the channel is the key here. RF information harvesting when other nodes transmit allows devices to break the symmetry between concurrently-transmitting devices based on the harvested energy from the ongoing transmissions. To demonstrate the benefits of RF information harvesting, we integrate it in a tailor-made ultra low-power MAC protocol we call *Radio Frequency-Distance Packet Queuing (RF-DiPaQ)*. We build a hardware/software prototype of RF-DiPaQ and devise a mathematical framework to study its performance at scale. Comparing RF-DiPaQ against staple contention-based MAC protocols, we show that it outperforms pure Aloha and 1-CSMA by factors of 3.55 and 1.21 respectively in terms of throughput, while it saturates at more than double the offered load compared to 1-CSMA. As traffic increases, the energy saving achieved by RF-DiPaQ against CSMA protocols increases, consuming 36% less energy than np-CSMA at high offered load, showcasing its ability to scale.

1 INTRODUCTION

Industry interest in wireless sensing is rising. For example, Airbus[1] is leading the efforts towards smart cabins, where wireless sensing is expected not only to contribute to better flying experiences but also to help airliners reduce costs. The losses for airliners due to mid-air injuries from falling baggage and severe turbulences as seat belts were not fastened and lost equipment are in the order of hundreds of millions of dollars, including lost workdays of crew[2]. Particularly, the crew is at risk during turbulences as they need to manually inspect if passengers have fastened their seat belts. Wireless sensing is expected to improve safety automatically by checking whether seat belts are fastened or overhead bins are properly latched.

Fig. 1 shows examples of this emerging class of wireless sensing event-driven applications. A large number of embedded devices are closely co-located and must rapidly report notifications regarding events of interest, for example, toggling a mechanical switch that signals a fastened seat belt, which are likely to occur almost simultaneously.

[1]https://www.airbus.com/newsroom/stories/iot-aerospace-great-new-connector.html (accessed: 2021-09-08)
[2]https://www.telegraph.co.uk/travel/travel-truths/products-you-can-take-from-an-airline/ (accessed: 2021-10-02)

* Corresponding author: N.H.Hokke@zed-iot.com.

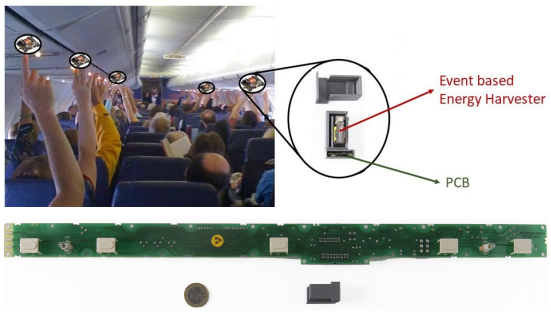

Fig. 1. Example of event-driven energy harvesting wireless sensing application: passengers flight attendant call buttons. The top figure shows our switch with 3D printed package. The bottom figure shows an actual PCB used for calling buttons in flights. The idea is to replace these with our miniature wireless event-driven energy-harvesting switches.

The notifications are to be reported wirelessly to a 1-hop gateway. However, the sensing devices cannot be powered through batteries due to safety regulations. If powered through cable harnesses, the increased fuel and maintenance costs would outweigh the advantages brought by wireless sensing [1]. The only alternative is to provision energy through ambient harvesting; yet, limited form factors pose extreme constraints on system design. The amount of energy harvested is minimal, for example, $\approx 200\,\mu$J from the operation of a mechanical switch, while the time for the harvested energy to completely dissipate is in the order of ms.

Moreover, unlike traditional embedded sensing, devices remain powered-off until the next harvesting event. While this work is in collaboration with a major aircraft OEM, this technology is applicable to other domains sharing similar features including logistics and industrial IoT. In these scenarios, vibrations may be used to power wireless sensors attached to packages that monitor physical quantities during travel [2] or embed sensor in the body of equipment in industries to measure vital operational parameters [3, 4].

Challenges. Due to stringent energy budgets, Aloha-like medium access protocols may appear as the natural choice. The simultaneity of event reporting, however, likely leads to contention on the wireless channel, eventually resulting in packet collisions and loss of event data. Handling channel contention through central coordination is plainly infeasible, due to the tiny energy budget that is likely sufficient for only a few transmissions, and unpredictable data generation times.

Opting for a Carrier-Sense Multiple-Access (CSMA) mechanisms may be an alternative. Still, because of the limited energy, devices can hardly afford the luxury of actively sensing the channel and harvested energy is likely to be insufficient to keep the node operational for long. Despite existing works on adaptive duty cycling for energy-harvesting sensors [5, 6] and specific MAC protocols

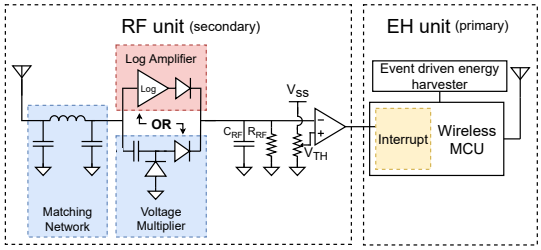

Fig. 2. Hardware schematic of an RF-DiPaQ sensor showing both the RF unit and the EH unit

for energy-harvesting wireless networks [7], batteryless energy-harvesting systems that are completely event-driven lack the fundamental mechanisms to handle channel contention.

RF information harvesting. We devise a notion of *radio-frequency (RF) information harvesting* to address these issues. Through special-purpose hardware support, the idea is to gain information on channel occupancy by harvesting energy from ongoing transmissions and break the symmetry between concurrently-transmitting devices. This provides ways to avoid collisions by deferring the upcoming transmissions differently at different devices.

To demonstrate the benefits of RF information harvesting, we integrate it in an ultra low-power MAC protocol expressly conceived for batteryless energy-harvesting event-driven wireless sensing that we call Radio Frequency-Distance Packet Queuing (RF-DiPaQ). Fig. 2 presents the hardware overview of a RF-DiPaQ sensor, where two coordinated units are integrated:

(1) *energy-harvesting (EH) unit*: it is the primary harvester, which scavenges energy from an event, stores it temporarily, and uses it only to transmit the event notification. The design involves harvesters transforming energy produced by an event into electrical energy, which is briefly stored in capacitors and used to power a transmitter reporting the event data. The harvested energy is thus barely sufficient to transmit a few packets only, without any energy left for other functionality.

(2) *radio-frequency (RF) unit:* it is the secondary harvester, which involves an RF-harvesting antenna, a matching circuit, and a reference capacitor circuit that effectively represents a hardware implementation of RF information harvesting. The harvesting antenna scavenges energy whenever other devices in the vicinity transmit a packet using a Wake-up Radio (WuR)-like receiver circuit charging the reference capacitor C_{RF}. This is otherwise discharged by resistor R_{RF}. When the reference capacitor C_{RF} discharges below a threshold, an idle channel is assessed, possibly triggering a packet transmission.

The incoming RF is amplified using either a voltage multiplier circuit comprising of passive components or a log amplifier (active device) as shown in Fig. 2. The log amplifier and voltage multiplier are mutually exclusive.

The main focus of this article is to exploit RF information harvesting and work around the extremely-tight energy constraints in order to design an effective medium access mechanism. The key to the efficient performance that RF information harvesting enables is in the functioning of the RF unit in situations of high channel contention. Because of the different packet transmission times, the spatial dispersion of transmitters, and varied path losses, the reference capacitors at C_{RF} at different RF-DiPaQ devices accumulate different amounts of energy. When discharging over resistor R_{RF}, the threshold triggering packet transmissions is crossed at different points in time at different devices. This introduces a form of temporal diversity that de-synchronizes packet transmissions, effectively resolving collisions.

Notably, *no additional energy* than the one used for packet transmissions is spent to this end. As new devices start transmitting while collisions are already occurring, the capacitors of the RF-DiPaQ devices whose reference capacitor voltage is still above the packet transmission threshold start charging again, pushing further the moment they attempt transmitting their packet. The processing repeats until the last RF-DiPaQ device transmits the pending packet. In a way, this mechanism is similar to the use of variable-sized colliding packet probes in receiver-initiated MAC protocols [8], but operates without the need of dedicated packet transmissions and thus incurs essentially no energy overhead.

Based on the operation of the RF unit, RF-DiPaQ devices refrain from transmitting until the medium is sensed idle, then transmit unconditionally, namely, they function akin to a 1-CSMA schema. However, contrary to 1-CSMA, which requires the medium to be continuously sensed by the device pending to transmit, RF-DiPaQ simply observes the reference capacitor voltage, which is charged by devices currently occupying the medium.

As a result of our design, networks using RF-DiPaQ enjoy the increased throughput offered by CSMA protocols, without the energy overhead of continuous channel sensing. Furthermore, contrary to CSMA protocols where channel sensing only occurs in the presence of pending transmissions, RF information harvesting is performed continuously: the reference capacitor constantly represents the current state of the channel, even before the main energy harvesting event occurs. This enables a node to gain a better snapshot of the channel conditions at the time an event occurs.

Contribution. Our *fundamental contributions* are to introduce the concept of RF information harvesting to monitor channel occupancy in real-time without using the primary harvester and to design an ultra low-power MAC protocol for networks of event-driven energy-harvesting wireless sensing devices that is incorporated into a hardware implementation, as illustrated in Sec. 3. A secondary novelty of this work is using the property of differential energy envelopes as a contention resolution mechanism over the existing RF harvesting/wakeup radio circuits. To the best of our knowledge, we are the first to turn RF energy harvesting into a channel sensing mechanism.

Next, our evaluation of the performance of RF information harvesting builds upon three pillars:
(1) an analytical model of the behavior of RF information harvesting in a low-power wireless protocol that allows us to determine performance at scale by deriving the probabilities of successful transmissions, throughput, and success rate, as illustrated in Sec. 4;
(2) a real-world hardware prototype, illustrated in Sec. 5, which doubles as an instrument to validate both the model of Sec. 4 and as a foundation for real-world experiments;
(3) a hybrid simulation environment, described in Sec. 6, created by combining a network simulator and an analog one, both required

	Throughput per Node	Normalized Throughput	Energy per Transmission	Overhead, feedback	Gateway Dependence	Semantic Addressing	Evaluation Type
Kwan [3]	6.4 bps	-	0.4-0.6 mJ	+2 B/pkt	High	Yes	**E, S**
Naderi [11]	320 bps	-	CS	RTS/CTS, ACK	Medium	No	**E, S**
Hoang [12]	-	0.45	CS	RTS/CTS, ACK, beacons	High	No	**N**
Bae [13]	-	0.16	CS	RTS/CTS, ACK	Medium	No	**N**
Ha [14]	40 bps	-	CS	RTS/CTS, ACK, beacons	High	Yes	**S**
Le [18]	64-68 bps	-	1.3-1.6 mJ	WuR-beacons, ACK	Medium	Yes	**S**
Karvonen [23]	64-68 bps	-	≈ 3.17 mJ	WuR-beacons, ACK	Medium	Yes	**S**
Oller [19]	144 bps	-	≈ 5.27 mJ	WuR-beacons, ACK	Medium	Yes	**S**
RF-DiPaQ	286 bps	0.64	0.4-0.6 mJ	zero	No	No	**E, S, N**

Fig. 3. Qualitative comparison of RF-DiPaQ with MAC protocols using RF harvesting or WuR receivers, the values of (normalized) throughput per node are at saturation. (E is Experimental, S is Simulated, N is Numerical).

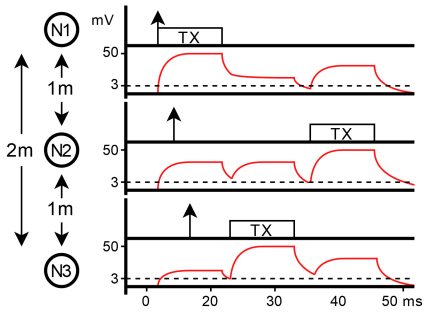

Fig. 4. RF activity and charge in C_{RF} over time for three transmitting nodes, under the RF-DiPaQ protocol.

to obtain accurate results as the operation of RF-DiPaQ extends across hardware and software.

Using the analytical model, the hybrid simulator, and the hardware prototype, we conduct an extensive evaluation of the performance of RF information harvesting when integrated in RF-DiPaQ. We report our findings in Sec. 7, for example, RF-DiPaQ outperforms pure Aloha and 1-CSMA by factors of 3.55 and 1.21 respectively in terms of throughput, while it saturates at more than double the offered load compared to 1-CSMA. As traffic increases, the energy savings achieved by RF-DiPaQ against CSMA protocols increase, consuming 36% less energy than np-CSMA at high offered load, showcasing its ability to scale.

2 RELATED WORK

Many works present RF harvesting solutions to partly cover the system's energy needs [9], using the same RF front-end for both energy harvesting and communication. The focus is on finding the optimal time division between harvesting and transmission to maximize throughput and energy efficiency [3, 10–14]. In contrast, we use RF harvesting as a channel sensing mechanism and the related hardware is exclusively used to that end; the choice of harvesting technology for the primary unit is orthogonal. Further, even though RF-DiPaQ is instrumental for us to show the applicability of RF information harvesting for channel sensing, the applicability of the latter extends beyond RF-DiPaQ. For example, receiver-initiated MAC protocols [8] often employ CCA-based rendezvous to reduce idle listening. RF information harvesting may be used as a replacement for that, reducing energy consumption and delay.

Our hardware implementation of RF information harvesting shares similarities with Wake-up Radios (WuR). Many WuR receivers exist using minimum active components with up to -56 dBm sensitivity while consuming around 1 μW in ISM bands [15–21]. WuR-based devices trigger the operation of the main computing and communication unit when a wake-up command is received on the WuR front-end [22]. The role of RF information harvesting is essentially different. Instead of requiring an explicit command to trigger the operation of another unit, RF information harvesting efficiently provides continuous information on channel occupancy using exclusively existing transmissions.

These fundamental building-blocks are often integrated into full-fledged MAC protocols to demonstrate the overall benefits, as we do when integrating RF information harvesting in RF-DiPaQ. For example, many MAC protocols are especially optimized for RF harvesting [3, 10–14] or use WuRs to reduce the energy cost of idle-listening [17–19, 23, 24]. Fig. 3 presents a qualitative comparison. Unlike our work, because of the single front-end used for energy harvesting and communication, protocols using RF harvesting struggle to adapt to changes in network topology, number of devices, and/or periodicity of transmissions. Further, not even when using WuR devices [17–19, 23], the energy consumed per transmission reaches the performance we achieve by using RF information harvesting in RF-DiPaQ.

Note that our system may be, in a sense, considered as an intermittent computing system [25]. However, the application processing in our case only includes a single atomic operation for transmitting the event data, and no application state is to be carried over to the next device activation. Therefore, the variety of techniques that use the persistent state to cross periods of energy unavailability are unnecessary here [26]. In a sense, RF information harvesting is also akin to backscatter communications [27]. RF information harvesting, however, is not in charge of communicating application data, regardless of the specific technique employed to that end, but merely acts as a channel sensing mechanism. Also, backscatter communications may not instantly catch the event and requires a more number of high-power transmitters to poll events, unlike RF-DiPaQ.

3 RF INFORMATION HARVESTING

The operation of our hardware implementation of RF information harvesting is deceptively simple. The received carrier wave is rectified by a RF harvesting circuit and used to charge a reference capacitor C_{RF}, which is continuously being discharged by a corresponding resistor R_{RF}, as shown in Fig. 2. This results in the voltage across C_{RF}, denoted by V_{RF}, to vary depending on channel activity. We compare V_{RF} to a close-to-zero voltage-threshold V_{TH}. When a carrier wave is being received, V_{RF} exceeds V_{TH}, indicating that a transmitter is utilizing the channel. With no carrier wave, V_{RF} drops below V_{TH}, indicating a clear channel.

The impact of this operation when integrated in a complete MAC protocol and at scale, however, is less straightforward. As we use RF information harvesting for channel sensing in RF-DiPaQ, the latter offers a way to investigate this aspect. In essence, RF-DiPaQ is a simple carrier-sense multiple access MAC protocol that uses RF information harvesting for channel sensing, and is especially optimized for that. It is the conceptual and practical instrument we use to investigate the impact of RF information harvesting on the whole system performance.

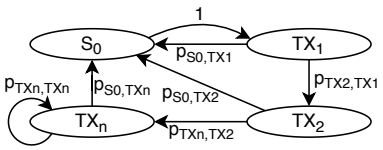

Fig. 5. Markov model of a network of RF-DiPaQ devices.

Fig. 4 illustrates an example execution, showing RF activity and the temporal variation of V_{RF} at three nodes, denoted as N1, N2, and N3. MAC frames arriving locally from higher layers in the stack are indicated by upward-pointing arrows and the *TX* block indicates packet transmissions. For simplicity of illustration, say the nodes are placed linearly 1 m apart and V_{TH} = 3 mV.

The first packet to arrive at N1 is transmitted immediately: V_{RF} is below the V_{TH} = 3 mV and so the channel is considered clear. As the transmission progresses, V_{RF} at the other two nodes grows according to the distance from N1; smaller distances imply higher voltage and vice-versa. Meanwhile, MAC frames arrive at N2 and N3 from the higher layers in the stack. Once N1's transmission is complete, V_{RF} at all nodes start dropping as the capacitor C_{RF} discharges over resistor R_{RF}.

Due to the lower initial value, V_{RF} of N3 drops below V_{TH} first. As a node with pending traffic checks the state of the channel before transmitting, N3 finds the channel clear before N2 and commences the transmission. This causes V_{RF} across the other two nodes to rise again, further postponing N2's transmission. Once N3 completes its transmission, V_{RF} at N2 eventually drops below V_{TH} too, causing N2's transmission to begin.

In principle, two or more nodes that experience the exact same propagation effects from a transmitter may reach the same V_{RF}, causing their transmissions to commence simultaneously, yielding a collision. In practice, due to multi-path fading and the presence of (moving) obstacles, these situations are extremely unlikely.

Note that channel sensing through RF information harvesting may occur independently of the MCU operation, even when the latter is not powered. The orthogonality of the two is reflected in the hardware design for RF-DiPaQ devices, depicted in Fig. 2. The EH unit is only dedicated to sensing and utilizes the RF unit strictly for channel sensing, while the two units remain decoupled also in energy provisioning. The antenna used for RF information harvesting may also be used to power the EH unit to reduce footprint, but due to the need for an RF switch, this would also decrease the receive sensitivity.

4 ANALYTICAL MODEL

The first asset we develop to study the benefits brought by RF information harvesting is a Markov model of a network of RF-DiPaQ devices. The model is instrumental to evaluate throughput and packet success rate for a given offered load g [28].

4.1 Model Overview

The model represents the behavior of the whole network and includes four states, shown in Fig. 5. In the S_0 state, there are no packets/events in the system and all charges in the reference capacitors C_{RF} are below V_{TH}. The S_0 state is always followed by TX_1, the first transmission state, as a result of the first packet generation and corresponding transmission. Following the first transmission,

From	To	Condition
S_0	TX_1	$\sum_P = 1 \wedge \forall c \in C : c < V_{TH}$
TX_1	S_0	$\sum_P = 0 \wedge \forall c \in C : c < V_{TH}$
TX_1	TX_2	$\sum_P > 0 \wedge min(C_p) = V_{TH}$
TX_2	S_0	$\sum_P = 0 \wedge \forall c \in C : c < V_{TH}$
TX_2	TX_n	$\sum_P > 0 \wedge min(C_p) = V_{TH}$
TX_n	S_0	$\sum_P = 0 \wedge \forall c \in C : c < V_{TH}$
TX_n	TX_n	$\sum_P > 0 \wedge min(C_p) = V_{TH}$

Fig. 6. Conditions for state transitions.

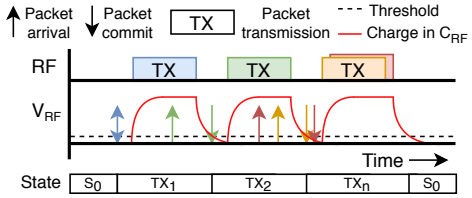

Fig. 7. Illustration of states transitions over time while packets arrive and its effect on V_{RF}.

in state TX_2 or TX_n the devices compare the charge in the reference capacitors C_{RF} against the threshold V_{TH}.

Fig. 6 summarizes the conditions for state transition, with $\sum_P$ being the total number of pending packets, C the set of charge levels in all reference capacitors C_{RF}, and $C_p \in C$ is the set of charges in the reference capacitors C_{RF} at nodes with pending packets. In the presence of pending packets, the moment the lowest charged capacitor hits V_{TH} and commits to transmit, the network transitions to the following transmission state. All states transition back to S_0 when there are no more pending packets and all capacitors are charged below V_{TH}. Fig. 7 shows an example execution illustrating how the time of packet arrivals, the time a node commits to transmit a packet, and discharge times align with the state transitions.

To quantify the network performance, we can calculate the system throughput T_h and packet success rate S as

$$T_h = \frac{\sum_{i=0}^{3} \pi^i \cdot T \cdot P(\text{success at } i)}{\sum_{i=0}^{3} \pi^i \cdot \underline{T^i}}, \tag{1a}$$

$$S = T_h / g, \tag{1b}$$

where g is offered load, π^i are the steady-state probabilities, T is packet transmission time, and $P(\text{success at } i)$ are the success probabilities at state i, with i being S_0, TX_1, TX_2, or TX_n.

In the following, we derive analytical expressions for steady-state probabilities π^i and the state success probabilities. In turn, these require quantifying the time for capacitor discharge and the duration of individual states.

4.2 Capacitor Discharge

Let us call T_{rc} the interval of time between the end of a transmission and the moment the charge in C_{RF} reaches V_{TH}.

This time depends on the amount of charge in C_{RF} accumulated during previous transmissions and until the end of the current transmission, on the *RC* value determined by C_{RF} and R_{RF} values, and on the value of V_{TH}. We express the charge in C_{RF} as the voltage level V due to input power P_{in} [16], $V = 10^{a \cdot P_{in} + b}$ with a, b being hardware constants.

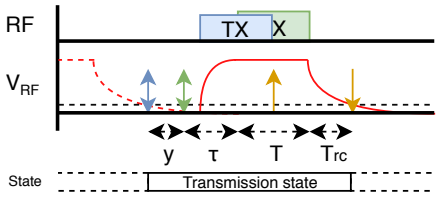

Fig. 8. Close-up view of a slice of Fig. 7 showing the individual time segments contributing to the duration of a state transmission.

Using the path-loss model, we express P_{in} as a function of distance d from the transmitter, resulting in

$$V = ld^k, \quad \text{where } k = -a10\gamma, l = 10^e, \\ e = a(P_{tx} - P_{l0} + 10\gamma log_{10}(d_0)) + b, \tag{2}$$

where the values of k and l may be empirically determined, γ is path loss exponent, P_{tx} is transmitted power, P_{l0} is path loss in decibels (dB) at the reference distance d_0.

As the discharge of C_{RF} follows an exponential RC curve, we express T_{rc} in terms of the value of a random variable D representing the distance from the transmitter

$$T_{rc} = \frac{RC}{T} \cdot ln\left(\frac{D^k \cdot l}{V_{TH}}\right) \tag{3}$$

Thus, T_{rc} may be seen as a transformation of a random variable D according to a certain function $h(d)$. If the distribution of D is known, we compute the probability density function (PDF) and cumulative distribution function (CDF) of T_{rc} as

$$f_{T_{rc}}(t) = -f_D(h^{-1}(t))\frac{\delta}{\delta t}h^{-1}(t), \tag{4}$$

$$F_{T_{rc}}(t) = 1 - F_D(h^{-1}(t)), \tag{5}$$

where indeed function h is the transformation of D into T_{rc}.

4.3 State Duration

The time spent in a transmission state is the sum of four time segments, as shown in Fig. 8, which together contribute to the expected time $\underline{T^i}$ spent in state i, thus

$$\underline{T^i} = \underline{y^i} + \tau + T + \underline{T^i_{rc}}, \tag{6}$$

where the individual quantities are determined as follows. As the radio takes time to stabilize before transmitting, there exists a *vulnerable time* between when a node finds the channel clear and when the transmission actually commences. Say the time for the radio to stabilize is r; we call $\tau = \frac{r}{T}$ the time for the radio to stabilize normalized to the packet transmission time T. Note that τ and T are constants determined by the chosen radio and packet structure. Because the reference capacitors are only charged when a transmission actually occurs, any other arrival within τ results in a collision. Therefore, y represents the difference in time between the first and last arrival within the vulnerable period τ. Finally, T_{rc} represents the discharge time at the lowest-charged node with pending packets; if no node has pending packets, it however represents the longest discharge time across the whole system.

In state TX_1, the CDF of y^{TX_1} equals the probability of no packet arrivals in the time interval $\tau - t$. The CDF can be differentiated to find the PDF, which determines the expected value of y^{TX_1} as $\underline{y^{TX_1}} = \tau - (1 - e^{-g\tau})/g$.

In state $TX_{\geq 2}$, y^{TX_2} and y^{TX_n} depend on the sum of the number of packets still pending and of the new packet arrivals within the τ interval experienced in the current state. The probability of the last discharge time to fall within time τ equals the PDF of $y^{TX_{\geq 2}}$, and as above it may be used to find the expected value of $y^{TX_{\geq 2}}$ as,

$$\underline{y^{TX_{\geq 2}}} = \sum_{n=2}^{N} P(N_{TX_{\geq 2}} = n) \int_{0+}^{\tau} t \cdot P(y^{TX_{\geq 2}} = t|n)dt, \tag{7}$$

$$P(N_{TX_{\geq 2}} = n) = \frac{\sum_{q=1}^{n} P(q \text{ in } \underline{T_{-1}} - \tau) \cdot P((n-q) \text{ in } \tau)}{\sum_{r=1}^{N}\sum_{q=1}^{r} P(q \text{ in } \underline{T_{-1}} - \tau) \cdot P((r-q) \text{ in } \tau)}, \tag{8}$$

which shows how to calculate the probability of having n pending nodes at time τ in the $TX_{\geq 2}$ states, where $P(x \text{ in } t)$ describes the probability of x arrivals in time t and stands for the Poisson PDF, and $\underline{T_{-1}}$ denotes the time duration of the previous state that equals $\underline{T^{TX_1}}$ and $\underline{T^{TX_2}}$ for TX_2 and TX_n, respectively.

When transitioning back to the S_0 state, T_{rc} takes is the longest discharge time across the whole system, as in this situation no nodes have pending packets waiting to be transmitted. The expected value of the maximum of multiple samples of the same distribution is found using order statistics [29] as $\underline{T_{rc,0}} = \int_0^\infty xNf_{T_{rc}}(x) \cdot F_{T_{rc}}(x)^{N-1}dx$, else, when at least one node has pending packets, T_{rc} is the discharge time of the lowest-charged node, which is calculated as $\underline{T_{rc,1}|n} = \int_0^\infty x \cdot n \cdot f_{T_{rc}}(x) \cdot (1 - F_{T_{rc}}(x))^{n-1}dx$.

To compute $\underline{T_{rc,1}}$, we need to determine the probability of a generic state ending with n nodes with pending packets. The packet arrivals during the first τ time of a generic state cause immediate transmissions, so this probability equals the probability of n arrivals in the remaining $\underline{T^i} - \tau$ time. As $\underline{T_{rc}}$ is yet unknown, an estimate is needed for $\underline{T^i} - \tau$.

For state TX_1, $\underline{T_{rc,0}}$ is used in the estimation of $\underline{T^{TX_1}} - \tau$ as given in Eq. 9. When the offered load g is small, the nodes are mostly in the TX_1 state, and the probability of transitioning to the S_0 state is higher than moving to TX_2, resulting in $\underline{T_{rc,0}}$. For state $TX_{\geq 2}$, we use $\underline{T_{rc,1}|n = 2}$ as an estimation to find $\underline{T^{TX_{\geq 2}}} - \tau$; $n = 2$ represents the smallest number of pending nodes resulting in the largest possible $\underline{T_{rc,1}}$.

$$\underline{T^{TX_1}} - \tau \approx \underline{T^{TX_1}_{\text{est}}} = \underline{y^{TX_1}} + T + \underline{T_{rc,0}} \tag{9}$$

$$\underline{T^{TX_{\geq 2}}} - \tau \approx \underline{T^{TX_{\geq 2}}_{\text{est}}} = \underline{y^{TX_{\geq 2}}} + T + \underline{T^{TX_{\geq 2}}_{rc,1}|n = 2} \tag{10}$$

Based on the estimates, the probability of the state ending with n pending nodes can be calculated. Given that the states end with one or more pending nodes, there must have been at least one, and at most N arrivals. So the probability of n arrivals must be divided by the sum of probabilities of one to N arrivals. This is calculated using the function $A(n, t, m)$ given by Eq. 11, which calculates the probability of n arrivals in time t, for at least m and at most N arrivals. Knowing the probabilities of ending with n arrivals for

each state, each $\underline{T_{rc,1}}$ is calculated based on the estimates as below,

$$P(N_{\underline{T_{\text{est}}}} = n) = A(n, \underline{T_{\text{est}}}, 1), \tag{11}$$

$$A(n,t,m) = \frac{P(n \text{ in } t)}{\sum_{i=m}^{N} P(i \text{ in } t)}, \tag{12}$$

$$\underline{T^i_{rc,1}} = \sum_{n=1}^{N} A(n, \underline{T^i_{\text{est}}}, 1) \cdot \underline{T^i_{rc,1}|n}. \tag{13}$$

With the expected value of $T^i_{rc,0}$ and $T^i_{rc,1}$ for all transmission states known, the $\underline{T_{rc}}$ can be calculated using Eq. 14. Where P^i_0 and P^i_1 are,

$$\underline{T^i_{rc}} = P_0 \cdot \underline{T_{rc,0}} + P_1 \cdot \underline{T^i_{rc,1}} \tag{14}$$

$$P^i_1 = 1 - P^i_0 = 1 - A(0, \underline{T^i_{\text{est}}}, 0). \tag{15}$$

With $\underline{y}$ and $\underline{T_{rc}}$ for all transmission states known, the average time spent in each state can be calculated using Eq. 6.

4.4 State Success Probability

As the reference capacitors in the TX_1 state are only charged time τ after the first arrival, any other arrival within time period τ will collide with the first packet. This results in the probability of success at the TX_1 state, P(s at TX_1), equaling the probability of no arrivals within τ, which is calculated with function $A(n,t,m)$ (Eq. 12) as, $P(\text{s at } TX_1) = A(0,\tau,0)$. The probability of success in the $TX_{\geq 2}$ states is based on the effect described in Sec. 3. The state is successful when the difference in discharge times of the two lowest charged nodes with a pending packet is larger than time τ (discharge time is modeled by T_{rc} as seen in Eq. 4 and Eq. 5). The probability of success knowing that n nodes are waiting to transmit at time τ in state, P(s at $TX_{\geq 2}$|n) is given in Eq. 16. Taking into account the probability of n pending nodes at time τ (Eq. 8) the probability of success for both $TX_{\geq 2}$ states, is represented by P(s at $TX_{\geq 2}$), and can be calculated as,

$$P(\text{s at } TX_{\geq 2}|n) = \int_0^{\infty} n \cdot f_{T_{rc}}(x) \cdot (1 - F_{T_{rc}}(x+\tau))^{n-1} dx \quad (\text{for } n \geq 1), \tag{16}$$

$$P(\text{s at } TX_{\geq 2}) = \sum_{n=1}^{N} P(N_{TX_{\geq 2}} = n) \cdot P(\text{s at } TX_{\geq 2}|n). \tag{17}$$

4.5 Steady State Probability

To calculate the model throughput and success rate, the steady state probabilities can be computed by solving linear equations resulting from all state transition probabilities (Fig. 5). The system can then be solved in terms of p_{TX_2,TX_1}, p_{TX_n,TX_2}, and p_{TX_n,TX_n}, which can be calculated using function $A(n,t,m)$ found in Eq. 12 as given in the following equations,

$$\begin{aligned} p_{TX_2,TX_1} &= 1 - P(\text{no arrivals in } \underline{T^{TX_1}} - \tau) \\ &= 1 - A(0, \underline{T^{TX_1}} - \tau, 0) \end{aligned} \tag{18a}$$

$$p_{TX_n,TX_2} = 1 - A(0, \underline{T^{TX_2}} - \tau, 0) \tag{18b}$$

$$p_{TX_n,TX_n} = 1 - A(0, \underline{T^{TX_n}} - \tau, 0) \tag{18c}$$

This now allows us to use Eq. 1a and Eq. 1b to model the throughput and success rate of RF-DiPaQ, at offered load g.

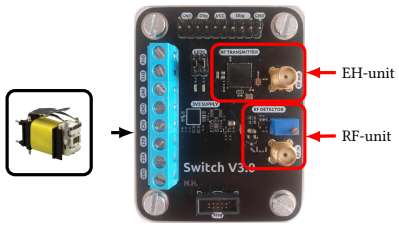

Fig. 9. Switch V3.0, our prototype wireless sensor running RF-DiPaQ with RF information harvesting.

5 PROTOTYPE

We build a hardware and software prototype to study the real-world behavior of RF information harvesting in RF-DiPaQ, shown in Fig. 9. We describe the system design next, along with the validation efforts that our prototype enables.

Hardware design.. Our Switch V3.0 can capture events when connected to mechanical harvesters, such as vibration and switches. Fig. 9 shows AFIG-0007 from ZF switches, a push-button type energy harvester module (ref. design from TI [30]). The energy generated by a single press and release of the button was measured on an average to be 420μJ. With this energy, our Switch V3.0 is functional up to one second.

To realize the RF unit, as shown in Fig. 2, we base our design on that of Nintanavongsa *et al.* [31]. The antenna is connected to a pi-matching network that tunes the RF unit to the specific carrier wave frequency. Using a mutually exclusive single-stage voltage multiplier and a log amplifier, the RF signal is rectified, doubled, and used to charge capacitor C_{RF}. The choice of selecting voltage multiplier or log amplifier is up to the designer depending on the use case. While voltage multiplier is completely passive, log amplifier requires power from the EH unit to function. However, log amplifier assists in sensing channel over longer ranges -up to 15 m when compared with voltage multiplier -up to 1.5 m. Hence, voltage multiplier can be used when the amount of harvested energy is relatively low and the nodes are nearby; log amplifier enables longer range at the cost of operating power.

Resistor R_{RF} discharges C_{RF} when no carrier wave is received. An inverting comparator compares the voltage in C_{RF} to the threshold voltage V_{TH}, which may be tuned through a potentiometer. The comparator outputs a digital high signal whenever the voltage in C_{RF} is lower than V_{TH} and a digital low signal otherwise. The digital output of the comparator is connected to an interrupt pin of the microcontroller unit (MCU).

We use TI's CC1352R [32] as MCU. We program the device to transmit event information immediately, as soon as the comparator output is high, or to sleep until a rising flank, and then transmit.

Sample execution. We replicate the scenario in Fig. 4 using three nodes N1, N2, and N3. N1 initially transmits a packet, whereas N2 and N3 trigger a new packet transmission while N1 is transmitting. As the three transmissions overlap in time within the same broadcast domain, this setting would normally cause collisions.

In contrast, Fig. 10 illustrates the operation of Switch V3.0 in this scenario. The plot shows the voltage measured over time across the capacitor of N2 (light blue) and N3 (dark blue), along with the digital output of the voltage comparators of N2 (teal) and of N3 (red). We indicate with C^n_{RF} the charge of the C_{RF} capacitor at node

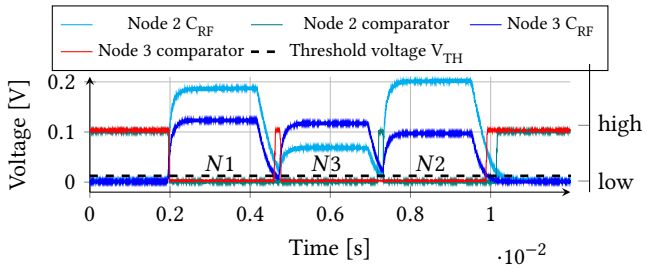

Fig. 10. The scenario of Fig. 4 with SWITCH V3.0 prototypes. The plot reports the measured voltage in the capacitors C_{RF} of N2 and N3 in Fig. 4, along with their digital comparator outputs (scaled down) over time.

Parameter	Value	Parameter	Value
V_{TH}	0.003 V	RC	0.0050 s
k	-1.146	T	0.01792 s
l	0.0334	τ	0.0084

Fig. 11. Model parameters, including those empirically determined using the SWITCHV3.0 prototype.

n. The initial transmission of N1, indicated with "1", makes the voltage levels at both C^2_{RF} and C^3_{RF} rise. As N2 is physically closer to N1 compared to N3, C^2_{RF} accumulates a higher charge. When N1 completes the transmission, the charge in both capacitors starts dropping, yet C^3_{RF} reaches the threshold voltage V_{TH} first.

The moment the voltage of C^3_{RF} is at V_{TH}, the comparator at N3 outputs a digital high signal, granting N3 permission to transmit. This transmission, indicated with "3" in the plot, causes the voltages in the capacitors to rise again, even before C^2_{RF} reaches V_{TH} while discharging. The voltage comparator at N2 consequently keeps emitting a digital low signal.

As soon as N3 completes the transmission, assuming N1 has no more packets pending, the voltage in C^2_{RF} eventually reaches V_{TH} while discharging, causing N2 comparator to output a digital high signal. As seen earlier for N3, this grants N2 permission to transmit. The transmission of N2, indicated with "2" in the plot, causes again all capacitors C_{RF} to charge. As there are no more packets to transmit, once N2 completes the transmission, the voltage levels of all capacitors C_{RF} eventually drop to zero, causing all comparators to output a digital high signal, indicating an idle channel.

Model validation. To instantiate the model of Sec. 4, we empirically determine the values of k and l in Eq. 2 by placing nine uniformly-spaced SWITCHV3.0 nodes on a line. We instruct them to transmit sequentially to the first node in the line, which measures the voltage across its capacitor C_{RF} for each received packet. This allows us to collect sparse knowledge on the relation between the voltage across C_{RF} and distance. We fit Eq. 2 to this data to find the k and l parameter. Further, in our prototype, the threshold voltage V_{tr} is set to 3 mV and the RC value to 0.0050 s. We use Eq. 4 and Eq. 5 to find the distribution of T_{rc}. With the SWITCHV3.0, a 100-byte packet yields a packet time of $T = 0.01792$ s; thus, the radio turn-on time normalized to the packet time results in $\tau = 0.0084$. Fig. 11 summarizes the model parameters we empirically determine.

We setup a network of thirty SWITCHV3.0 nodes, placed within a sixteen square-meter area with the gateway close to the middle, as shown in Fig. 12. The nodes are powered using batteries and

Fig. 12. A network of 30 SWITCHV3.0 nodes and gateway in a 4 m by 4 m area emulating multiple harvester events per second.

emulate multiple harvester events at all thirty nodes. All nodes are programmed to generate X packets at a $g/9$ Poisson arrival rate. The gateway measures the ratio of successfully received packets. The success rate at a particular g is multiplied by g to obtain the network throughput.

Based on the model parameters in Fig. 11 and the Euclidean distances between the nodes in the setup of Fig. 12, we numerically compute expected state times $\underline{T^i}$, state success probabilities $P(\text{success at } i)$, and steady state probabilities π^i for a given offered load g. Then, using Eq. 1a and Eq. 1b we find the model throughput and success rate at load g for the considered network topology. We apply a similar procedure to compare the behavior of RF-DiPaQ with the expected performance of 1-CSMA, ALOHA, and np-CSMA determined using existing models [28].

Fig. 13 shows the results. The model success rate and throughput for RF-DiPaQ closely follow the measured data. However, when approaching $g = 30$ and higher, the throughput in the actual protocol performance decreases, unlike the model. This happens because no higher arrival rate than $g = 30$ is possible in our network of 30 nodes. At higher values of offered load g, the performance of RF-DiPaQ is limited by the average C_{RF} discharge time of the lowest charged node with pending traffic, as this equals the non-utilized time between two consecutive transmissions. Thus, throughput of RF-DiPaQ network is expected to approach zero at high values of g.

Fig. 13 also demonstrates that the performance of RF-DiPaQ is generally better than ALOHA and similar to 1-CSMA only up to $g = 10^0$. After that, RF-DiPaQ outperforms 1-CSMA, confirming the expectation of RF-DiPaQ superiority in higher traffic. However, the system throughput, as shown in Fig. 13, remains constant after $g = 10^0$, whereas the performance of np-CSMA continues to improve. The plateau exists due to the relatively small number of nodes, which reduces the number of different voltages the capacitors C_{RF} are charged to. As the throughput is limited by the average discharge time between two successive transmissions and this does not depend on offered load, the throughput remains constant thereafter. On the other hand, np-CSMA would achieve this performance by spending more energy than RF-DiPaQ. We return to energy performance in Sec. 7.

6 HYBRID CIRCUIT-NETWORK SIMULATOR

While the prior graphs were obtained on the prototype devices, setting up a large-scale experimental testbed using hardware prototypes that is representative of the characteristics of the applications we target is arguably difficult. In particular, executing repeatable controlled experiments is hard, because gaining the required level of visibility into the system operation becomes a challenge when the system operation is a mixture of digital and analog functionalities. Monitoring the charge and discharge of C_{RF}, for example, without

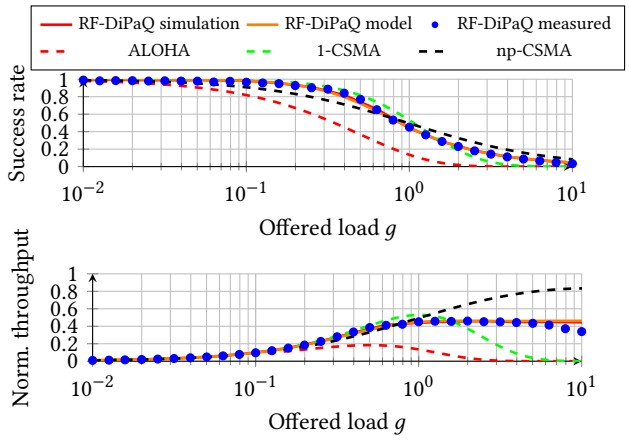

Fig. 13. Success rate (top) and normalized throughput (bottom) of the configuration in Fig. 12 comparing RF-DiPaQ model, RF-DiPaQ measurement, and baseline protocols according to their respective models [28].

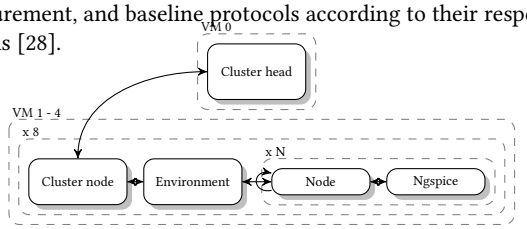

Fig. 14. High level view of the hybrid Circuit–Network simulator.

affecting the energy patterns can become increasingly impractical at large-scale.

Simulator overview. To enable an accurate, yet extensive evaluation of RF-DiPaQ, as reported in Sec. 7, we extend the open-source analog simulator Ngspice with a custom agent-based network simulator written in Python. The combination of the two allows to simulate both the analog circuitry and network capabilities of RF-DiPaQ nodes at once. Using the simulator we can quantitatively study aspects, such as the limiting conditions of throughput, and the effects of different node placements. The simulator is implemented to operate in a distributed fashion across multiple Virtual Machines (VMs), allowing to simulate multiple scenarios in parallel, which is needed to run the computationally heavy analog simulators in a timely manner. Using a SPICE script, the analog circuit of the RF-unit can be loaded into the simulator. When the analog circuit is not known, the relation between input power and DC output voltage may be supplied according to Eq. 2.

Fig. 14 shows a high level system overview of the simulator. The simulation scenario is configured with a specific hardware setup, node layout, and ranges of packet generation rates. The cluster head coordinates the simulation setup across VMs, distributing the configured setup to the cluster nodes. Each of these configures an environment with N nodes based on the given configuration. Each of the N nodes is configured with the Ngspice reference model or DC output voltage.

Simulator functioning. Fig. 15 is a snapshot of a simulation showing the RF activity of nine nodes over time, and their effect on the C_{RF}s, following the RF-DiPaQ protocol. During the simulation, the simulated wireless devices interact with each other, indicating when each device starts or stops transmitting. Based on the distance to

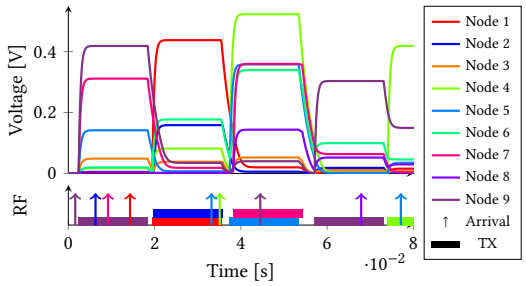

Fig. 15. The voltage levels in the reference capacitors C_{RF} of nine nodes reacting to the RF activity over time, behaving according to RF-DiPaQ.

the transmitter(s) and pathloss model, the simulator determines the voltage level that C_{RF} reaches. Based on this, transmissions are made following the RF-DiPaQ protocol.

For validation, we simulate the scenario described in Sec. 5 and shown in Fig. 12, already employed to validate the model of Sec. 4. Fig. 13 also reports the simulated success rate and throughput for RF-DiPaQ. The trends obtained from the simulator closely match the model and measurement results. However, since in the simulation a node may generate a packet while transmitting, the network can reach an offered load of $g = 10^1$ and higher without a decrease in throughput.

7 EVALUATION

In this section, we evaluate the performance of RF-DiPaQ on a network of SwitchV3.0 nodes. We model and simulate, how state-of-the-art WuR front-end hardware would perform if used as RF-unit, show how the optimal RC value can be found, and compare the energy consumption of RF-DiPaQ to the CSMA protocols and classic Aloha. We also discuss how RF-information harvesting may be used outside event-based batteryless wireless sensing. Most of our evaluation is primarily obtained from the testbed of devices, unless explicitly mentioned.

7.1 Transmission Distance

To test the effect of distance between neighboring devices on the performance of the RF-DiPaQ protocol, nine Switch V3.0 RF-DiPaQ enabled nodes (Fig. 9) were placed in a 3 by 3 grid and tested for different grid-neighbor (inter node) distances, ranging from 25 cm to 15 m. We evaluate Switch V3.0 using both voltage multiplier and log amplifier separately, as they affect the node to node sensing distance achieved. Fig. 16 shows the success rate and the normalized throughput of different grid sizes of 9 nodes with voltage multiplier. As expected, when using large device-to-device distances (150 cm for the Switch V3.0) the RF-units of the nodes cannot sense the transmissions of other nodes, and the performance of the RF-DiPaQ is reduced to the performance of Aloha. This showcases the effect of the increase in the number of hidden terminals to the throughput of RF-DiPaQ. Further, as observed in Fig. 16, the shortest grid-neighbor distance does not result in the best performance. 50 cm outperforms 25 cm, because in the 25 cm layout, the reference capacitors C_{RF} of the nodes are charged to relatively higher voltages, resulting in longer average discharge times T_{rc} between two successive transmissions which cannot be utilized, reducing the throughput.

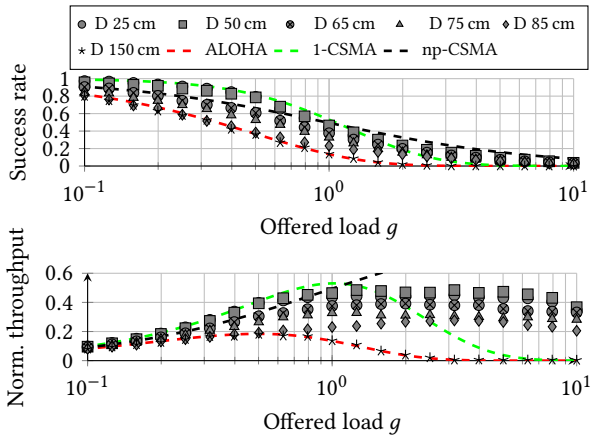

Fig. 16. Measured success rate (top) and normalised throughput (bottom) of 3 by 3 grid of 9 nodes for different node distances with voltage multiplier

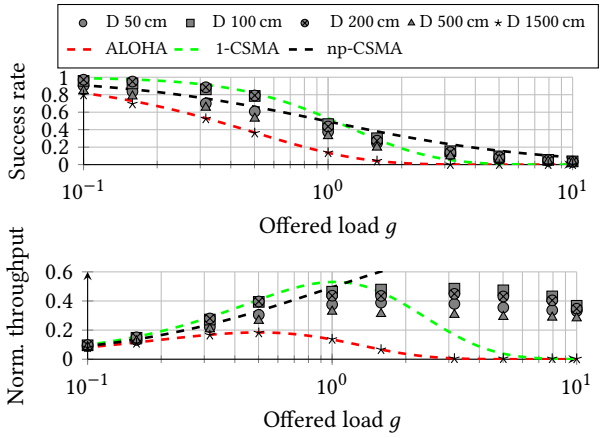

Fig. 17. Measured success rate (top) and normalised throughput (bottom) of 9 nodes for different node distances with log amplifier.

Fig. 17 shows the success rate and normalized throughput of different grid sizes of 9 nodes when log amplifier is employed. As expected, in this case the nodes can sense transmissions at greater distances (up to 200 cm), and the number of hidden terminals decreases due to enhanced node sensitivity. Furthermore, the performance degrades at larger distances (from 5 m) as transmissions from nodes farther away can no longer be detected. Similar to the voltage multiplier results, at smaller grid-neighbor distances (of less than 200 cm in this case), the network throughput is reduced due to longer discharge times T_{rc}.

These results demonstrate a trade-off in terms of the energy used by the node for sensing the channel and the achieved sensitivity to other transmissions. Hence, depending on the available harvested energy and the sensing distance required for a particular use case, the choice between voltage multiplier or log amplifier can be made.

7.2 RF Unit

The performance of RF-DiPaQ depends on the RF-unit efficiency of harvesting the carrier wave and charging the capacitor. As the hardware used in WuR front-ends shares many similarities with the RF-unit, they can be re-purposed to serve as RF-unit in RF-DiPaQ scenario. Due to the unavailability of state-of-the-art WuR hardware, the model and simulation can be used to evaluate how WuR hardware would perform while serving as RF-unit. In specific, only the minimal sensitivity and the relation between DC output voltage V_{out} and input power P_{in} are needed. This allows to model the performance of the microwatt-WuR proposed by Del-Prete *et al.* [16] if adapted to serve RF-DiPaQ functionalities. The relation between V_{out} and P_{in}, is given in Eq. 19, and holds for $P_{in} \in [-70\,dBm, -35\,dBm]$. The minimal sensitivity of this hardware results in $V_{TH} = 300\,\mu V$ at an input power of -56 dBm.

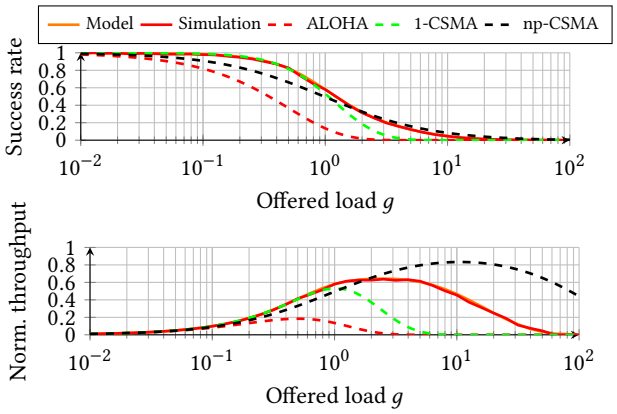

Fig. 18. Modeled success rate (top) and normalized throughput (bottom) of 100 nodes in a grid layout in a 25 m × 25 m area.

$$V_{out} = 10^{aP_{in}+b}, \text{ with } a = 0.100993, b = 2.132736 \quad (19)$$

Fig. 18 shows the performance of RF-DiPaQ regarding model and simulation using 100 nodes. The nodes are positioned into a 10 by 10 node grid layout spread across a 25 m by 25 m area. Prospective use-cases involving EH-device distributions like the above can be seen inside smart factories where tens/hundreds of sensors are positioned in a few square meters and need to transmit information regarding the structural health of machinery [33] or in cases of on-demand transmissions like the ones depicted in Fig. 1 (call-crew buttons) [34]. In terms of our grid layout, the minimum distance between any pair of nodes in the network equals 2.78 m, resulting in a maximum P_{in} of less than -35 dBm, within the P_{in} range.
As shown clearly in the success rate in Fig. 18, RF-DiPaQ outperforms np-CSMA for 100 nodes and follows the 1-CSMA performance, until an offered load of $g = 0.8$. As seen in the throughput in Fig. 18, after $g = 0.8$ RF-DiPaQ outperforms 1-CSMA with a max normalized throughput of 0.64 at the saturation point $g = 2.51$, compared to 0.53 at $g = 1$ for 1-CSMA. The network under RF-DiPaQ can handle 2.46 times more offered load than 1-CSMA and 4.74 times more than Aloha in saturation. RF-DiPaQ achieves a throughput of 1.21 times more than 1-CSMA, while not consuming energy for carrier sensing, contrary to the continuous sensing in 1-CSMA. Further, RF-DiPaQ performs better than np-CSMA for lower traffic loads, i.e., till saturation. Using the same number of RF-DiPaQ nodes in smaller grids would lead to saturation at even higher values of g. As the probability of collisions depends on the standard deviation of T_{rc}, a smaller RC value could be used while maintaining the standard deviation, but reducing the mean. This would reduce the unutilized time between two successive transmissions while maintaining the probability of collisions, thus increasing the saturation point.

This model and simulation are based on the hardware of -56 dBm WuR [16], as from this hardware the relation between V_{out} and P_{in} became known. Although there are more sensitive WuR designs, like the -79.1 dBm WuR proposed by Mangal *et al.* [35], their relation between V_{out} and P_{in} is not known and, therefore, cannot be modeled or simulated in networks of RF-DiPaQ nodes. Nevertheless, RF-DiPaQ nodes with a -79.1 dBm RF-unit would result in a significantly larger range. The RF-DiPaQ MAC protocol does not need semantic-addressing; just the carrier wave detection. Thus, no sensitivity has to be used to decode the wake up call. Therefore, the hardware of the state-of-the-art WuRs [17, 24, 35, 36] achieves even higher sensitivity when used as RF-units in RF-DiPaQ scenarios.

7.3 Energy Consumption

RF-DiPaQ also outperforms 1-CSMA regarding energy usage. Regarding throughput in Fig. 18, when RF-DiPaQ saturates at an offered load of $g = 2.51$, nodes following 1-CSMA spend on average 60% of the packet time T sensing the medium, waiting to transmit. This results in 1.7 times higher energy usage than in RF-DiPaQ. Fig. 19 shows the power trace of the Switch V3.0 (Fig. 9) while waking up to transmit/sense the channel, showing the power consumption for transmitting and carrier sensing to be 22 mW and 27 mW, respectively. For this hardware, the average energy usage per arrival equals 689.5 μJ in 1-CSMA and 410.26 μJ in RF-DiPaQ, as seen in Fig. 20. Apart from the above mentioned amount of saved energy which is due to zero energy sensing, RF-DiPaQ also evades collisions by prioritizing transmissions based on distance. These collisions would lead 1-CSMA to consume more energy having to retransmit.

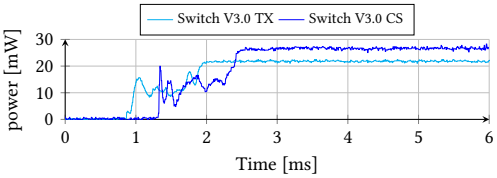

Fig. 19. Measured power consumption of the Switch V3.0, while waking up from sleep into TX and Carrier Sensing mode.

Regarding np-CSMA, energy consumption due to sensing depends on the frequency and duration of sensing (i.e., back-off intervals). Assuming a CCA of 0.15 ms, the Switch V3.0 consumes a minimum of 20.66 μJ per assessment. The probability of a packet arriving at a busy medium equals $p = 1/(1+1/g)$. Using the expected value of the geometric distribution, the expected number of failed assessments before transmitting can be calculated to $(1/(1-p))-1$. For the Switch V3.0 hardware at an offered load of $g = 2.51$ this results in 2.51 tries before transmitting, resulting in an average of 486.72 μJ consumed per packet. This amount still exceeds the consumed energy per packet of RF-DiPaQ, as seen in Fig. 20. As traffic load g increases RF-DiPaQ outperforms the CSMA protocols by a higher factor regarding energy consumption. For example, at $g = 5$, wherein the throughput of the 100 nodes simulated in Sec. 7.2 is still above 0.6, 1-CSMA and np-CSMA consume 796.9 μJ and 513.56 μJ, respectively, while the consumption of RF-DiPaQ remains the same, as shown in Fig. 20. When specifically compared to np-CSMA, RF-DiPaQ consumes 36% less energy at an offered load of $g = 5$, while 10% less at $g = 1.5$.

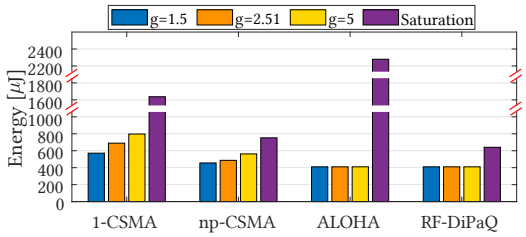

Fig. 20. Energy per packet transmission for different MAC protocols for different offered load values.

7.4 Effect of placement on Fairness

As RF-DiPaQ orders nodes based on the charge in their capacitors, nodes that are charged higher more often get the chance to transmit less often. This results in unfairness for the nodes in the high density parts of deployment. For a network laid out in a grid this results in nodes in the middle of the network having poor performance since these nodes see more often a close-by neighbor transmitting compared to nodes at the edge of the network. This unfairness due to position can however be corrected by adapting T_{rc} – the RC discharge parameter. By increasing the RC values for the nodes near the edge of the network, their discharge time is increased to equal the discharge time of the nodes in the middle of the network that are charged to a higher value.

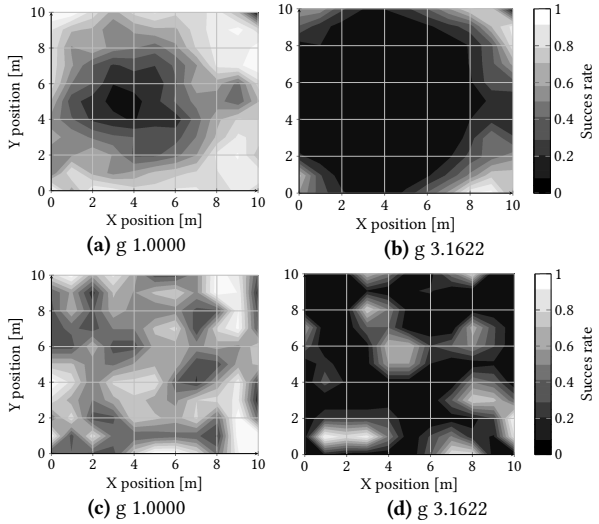

Fig. 21. Positional fairness for load g = 1.000 (a and c) and g = 3.1622 (b and d), for a network without RC correction (a and b) and with RC correction (c and d), showing the positional unfairness and the effect of the correction.

We performed multiple experiments on our simulation platform to find insight regarding the unfairness. The effect of this correction is shown Fig. 21, Where the top-two sub-figures show the lack of fairness without the RC correction, and the bottom-two the fairness with the RC correction. As expected without the RC correction, nodes in the middle of the network are disadvantaged and perform poorly. While with the RC correction the performance of a node does not depend on its location.

7.5 Selection of R_{RF} and C_{RF}

To optimize RF-DiPaQ performance the optimal RC value needs to be found. Besides the threshold level and the voltage to which the reference capacitors C_{RF} are charged, the RC value affects the discharge time. A relatively larger RC value results in longer average discharge times. As the discharge time between two successive transmissions cannot be utilized this limits the network throughput. Apart from the average discharge time, the RC value also influences its variance. Lower RC values result in a smaller discharge time variance, increasing the probability of two pending nodes having the same discharge time, causing a collision.

Fig. 22 shows the effect of the RC value on the T_{rc} discharge distribution calculated with Eq. 5. A larger RC value both increases the mean and deviation of T_{rc}. However, a lower average discharge

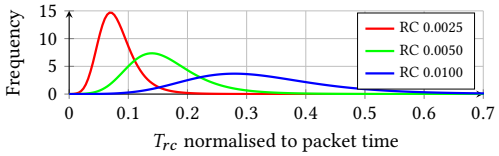

Fig. 22. T_{rc} distribution of a large network for different RC values.

time also lowers the probability of an arriving packet finding a busy medium. At low values of offered load g this increases the success rate, making RF-DiPaQ match 1-CSMA as shown in Fig. 23 for RC values up to 1ms. The optimal RC value is small enough to not result in overly large average discharge times, and large enough to not result in many collisions. Finding the optimal RC value can be done by modeling a range of different values. Fig. 23 presents the success rate and throughput of the Switch V3.0 in the scenario described in Sec. 5 for different RC values and shows how the optimal RC value for the Switch V3.0 was found. As seen in the throughput in Fig. 23, the RC value of 0.0050 s results in optimal performance. When the RC value is increased (0.0100 s and 0.0200 s) the maximum throughput is reduced. When the RC value is decreased (0.0010 s and 0.0005 s) the probability of collisions increases, reducing the throughput at higher levels of offered load g.

7.6 Influence of noise

The selected comparator (TS881 by Mouser) has an input hysteresis of 2.4 mV, which prevents its output from oscillating between both rails, due to the effect of noise, when the input voltage matches the reference voltage. Noise however affects the minimum charge levels across C_{RF}, i.e., V, as the in-band noise floor charges the capacitors. If V is always above V_{TH} then the node assumes the medium is busy and never transmits, if it is below V_{TH} the node is unaffected. As V_{TH} is tunable, it can be tuned in noisy environments to circumvent this issue.

Noise also has an effect on the charge level while receiving a transmission, affecting the discharge time. To evaluate this, two nodes were placed at 10 cm distance, one programmed to transmit and the other to measure and report its discharge times, $T_{rc}^{(1)}$, which is the T_{rc} of a single transmitter-receiver pair. $f_{T_{rc}^{(1)}}$ and $F_{T_{rc}^{(1)}}$ are the PDF and CDF of the Gaussian fit. The probability of collision of two nodes at equal distance from the previous transmitter is,

$$P_{ceq} = \int_0^\infty f_{T_{rc}^{(1)}}(x) \cdot (F_{T_{rc}^{(1)}}(x+0.008) - F_{T_{rc}^{(1)}}(x-0.008))dx. \quad (20)$$

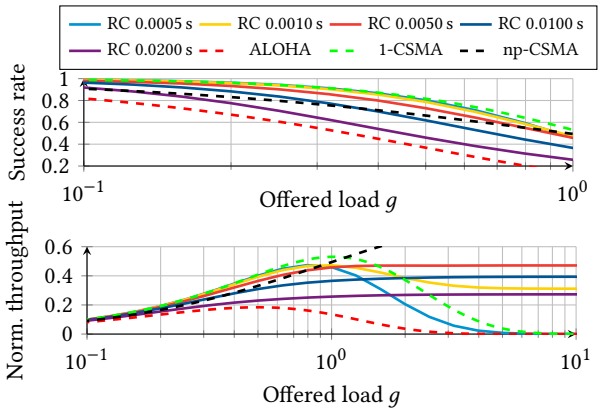

Fig. 23. Success rate (top) and normalized throughput (bottom) of nine nodes in a grid layout of 1 m×1 m for different RC values.

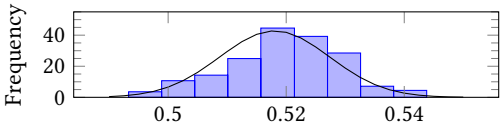

Fig. 24. Effect of noise on measured discharge time, $T_{rc}^{(1)}$, of a single node receiving from a single transmitter; Gaussian fit with the standard deviation of 0.009.

Fig. 24 shows the measured discharge times and the effect of noise on the deviation. By fitting a Gaussian distribution, we found Standard deviation to be 0.009. With $\tau = 0.0084$ (see Sec. 4.3), which is the time two nodes must differ in discharge times to avoid a collision, P_{ceq} is 0.455. However, the probability of two nodes being exactly equidistant from a transmitter is very low and decreases exponentially with the number of nodes, e.g., with 10 nodes it is 0.0003. RF-DiPaQ will be affected by external sources transmitting on the same channel very close to the deployment, which is a known limitation. However, this is not a concern for our current applications within aircraft cabins.

7.7 Effects of multipath

As expected, RF-DiPaQ performs well in clear environments. But even in multipath scenarios its performance does not deteriorate. The randomness inserted in the charging level across C_{RF} of the nodes increases the deviation of T_{rc} without increasing the mean (Sec. 7.5), resulting in better performance. Fig. 26 shows the mea-

(a) Multipath effect in Fuselage **(b)** Open field

Fig. 25. Setup in different terrains.

sured success rate and normalized throughput of the same network in fuselage of an aircraft and open field. Due to low sensitivity of the Switch v3.0 nodes, the benefit of multipath is only small. As RF

waves bounces of nearby object often doubles the distance between transmitter/receiver exceeding the minimum sensitivity resulting in limited differences.

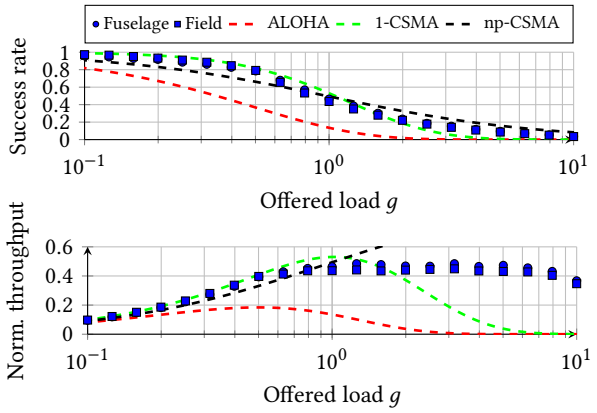

Fig. 26. Measured success rate (top) and normalised throughput (bottom) of a network of 9 nodes inside a fuselage and outside in an open field Fig. 25, showing the effect of multipath.

8 CONCLUSION

RF information harvesting allows wireless embedded sensing devices to detect channel activity at essentially no energy cost. This feature becomes an asset in an emerging class of event-driven energy harvesting and wireless sensing applications, composed of energy-harvesting batteryless devices operating with tiny energy budgets. The RF-DiPaQ protocol integrates RF information harvesting to sense the medium and prioritize devices regarding channel access based on distance from the current transmitter. We detailed and analytically modeled the design of RF-DiPaQ, as well as created a real-world hardware/software prototype called SwitchV3.0. We also developed a hybrid circuit-network simulator to evaluate the protocol performance in conditions as close to reality as possible, yet without the practical limitations due to setting up repeatable controlled experiments.

Our results indicate that RF-DiPaQ outperforms 1-CSMA with a maximum normalized throughput of 0.64 at the saturation point $g = 2.51$, compared to 0.53 at $g = 1$ for 1-CSMA. The network under RF-DiPaQ can handle 2.46 times more offered load than 1-CSMA and 4.74 times more than Aloha in saturation. Furthermore, when compared to np-CSMA, which is best performing among p-CSMA, np-CSMA and 1-CSMA for high offered loads, RF-DiPaQ consumes 36% less energy at offered load $g = 5$, while 10% less at $g = 1.5$.

9 ACKNOWLEDGEMENT

InSecTT has received funding from the ECSEL Joint Undertaking (JU) under grant agreement No 876038. The JU receives support from the European Union's Horizon 2020 research and innovation programme and Austria, Sweden, Spain, Italy, France, Portugal, Ireland, Finland, Slovenia, Poland, Netherlands, Turkey. The document reflects the author's view only and the Commission is not responsible for any use that may be made of the information it contains.

REFERENCES

[1] S. Sudevalayam and P. Kulkarni, "Energy harvesting sensor nodes: Survey and implications," *IEEE Comm. Surveys and Tutorials*, vol. 13, no. 3, pp. 443–461, 2011.
[2] S. Gună, L. Mottola, and G. P. Picco, "Dice: Monitoring global invariants with wireless sensor networks," *ACM Trans. on Sensor Networks*, vol. 10, no. 4, 2014.
[3] J. C. Kwan and A. O. Fapojuwo, "Radio Frequency Energy Harvesting and Data Rate Optimization in Wireless Information and Power Transfer Sensor Networks," *IEEE Sensors Journal*, vol. 17, no. 15, pp. 4862–4874, 2017.
[4] J. C. Rodriguez, V. Nico, and J. Punch, "Powering wireless sensor nodes for industrial iot applications using vibration energy harvesting," in *2019 IEEE 5th World Forum on Internet of Things (WF-IoT)*, 2019, pp. 392–397.
[5] A. Kansal, J. Hsu, S. Zahedi, and M. B. Srivastava, "Power management in energy harvesting sensor networks," *ACM Transactions on Embedded Computing Systems (TECS)*, vol. 6, no. 4, pp. 32–es, 2007.
[6] S. Ulukus, A. Yener, E. Erkip, O. Simeone, M. Zorzi, P. Grover, and K. Huang, "Energy harvesting wireless communications: A review of recent advances," *IEEE JSAC*, vol. 33, no. 3, pp. 360–381, 2015.
[7] H. H. R. S. et al., "A comprehensive review on energy harvesting MAC protocols in WSNs: Challenges and tradeoffs," *Ad Hoc Networks*, vol. 71, 2018.
[8] M. L. Wymore and D. Qiao, "RIVER-MAC: A Receiver-Initiated Asynchronously Duty-Cycled MAC Protocol for the Internet of Things," in *2019 IEEE 43rd Annual Computer Software and Applications Conference*, vol. 1, 2019, pp. 860–869.
[9] X. L. et al., "Wireless Networks With RF Energy Harvesting: A Contemporary Survey," *IEEE Comm. Sur. and Tut.*, vol. 17, no. 2, pp. 757–789, 2015.
[10] J. Ren, J. Hu, D. Zhang, H. Guo, Y. Zhang, and X. Shen, "RF Energy Harvesting and Transfer in Cognitive Radio Sensor Networks: Opportunities and Challenges," *IEEE Communications Magazine*, vol. 56, no. 1, pp. 104–110, 2018.
[11] M. Y. Naderi, P. Nintanavongsa, and K. R. Chowdhury, "RF-MAC: A Medium Access Control Protocol for Re-Chargeable Sensor Networks Powered by Wireless Energy Harvesting," *IEEE Trans. on Wireless Comm.*, vol. 13, no. 7, pp. 3926–3937, 2014.
[12] D. T. Hoang, D. Niyato, P. Wang, and D. I. Kim, "Opportunistic Channel Access and RF Energy Harvesting in Cognitive Radio Networks," *IEEE JSAC*, vol. 32, no. 11, pp. 2039–2052, 2014.
[13] Y. H. Bae and J. W. Baek, "Sensing Strategy Exploiting Channel Memory in CR Network With RF Energy Harvesting," *IEEE Communications Letters*, vol. 22, no. 12, pp. 2539–2542, 2018.
[14] T. Ha, J. Kim, and J. Chung, "HE-MAC: Harvest-Then-Transmit Based Modified EDCF MAC Protocol for Wireless Powered Sensor Networks," *IEEE Transactions on Wireless Communications*, vol. 17, no. 1, pp. 3–16, 2018.
[15] M. Magno, V. Jelicic, B. Srbinovski, V. Bilas, E. Popovici, and L. Benini, "Design, Implementation, and Performance Evaluation of a Flexible Low-Latency Nanowatt Wake-Up Radio Receiver," *IEEE Transactions on Industrial Informatics*, vol. 12, no. 2, pp. 633–644, 2016.
[16] M. Del Prete, A. Costanzo, M. Magno, D. Masotti, and L. Benini, "Optimum Excitations for a Dual-Band Microwatt Wake-Up Radio," *IEEE Transactions on Microwave Theory and Techniques*, vol. 64, no. 12, pp. 4731–4739, 2016.
[17] D. Spenza, M. Magno, S. Basagni, L. Benini, M. Paoli, and C. Petrioli, "Beyond duty cycling: Wake-up radio with selective awakenings for long-lived wireless sensing systems," in *IEEE ICC*, 2015, pp. 522–530.
[18] T. N. Le, M. Magno, A. Pegatoquet, O. Berder, O. Sentieys, and E. Popovici, "Ultra Low Power Asynchronous MAC Protocol Using Wake-up Radio for Energy Neutral WSN," in *Proceedings of the 1st International Workshop on Energy Neutral Sensing Systems*. Association for Computing Machinery, 2013.
[19] J. Oller, I. Demirkol, J. Casademont, J. Paradells, G. U. Gamm, and L. Reindl, "Wake-up Radio as an Energy-Efficient Alternative to Conventional Wireless Sensor Networks MAC Protocols," in *Proc.of 16th ACM International Conference on Modeling, Analysis & Simulation of Wireless and Mobile Systems*. ACM, 2013.
[20] M. Zgaren and M. Sawan, "A high-sensitivity battery-less wake-up receiver for 915 MHz ISM band applications," in *IEEE ICECS*, 2015, pp. 336–339.
[21] J. M. et al., "A -106dBm 33nW Bit-Level Duty-Cycled Tuned RF Wake-up Receiver," in *2019 Symposium on VLSI Circuits*, 2019, pp. C86–C87.
[22] C. S. et al., "Optimizing sensor networks in the energy-latency-density design space," *IEEE Trans. on Mob. Comp.*, vol. 1, no. 1, pp. 70–80, 2002.
[23] H. Karvonen, J. Petäjäjärvi, J. Iinatti, M. Hämäläinen, and C. Pomalaza-Ráez, "A generic wake-up radio based MAC protocol for energy efficient short range communication," in *2014 IEEE 25th Annual International Symposium on Personal, Indoor, and Mobile Radio Communication (PIMRC)*, 2014, pp. 2173–2177.
[24] D. Ghose, F. Y. Li, and V. Pla, "MAC Protocols for Wake-Up Radio: Principles, Modeling and Performance Analysis," *IEEE Transactions on Industrial Informatics*, vol. 14, no. 5, pp. 2294–2306, 2018.
[25] B. Lucia, V. Balaji, A. Colin, K. Maeng, and E. Ruppel, "Intermittent computing: Challenges and opportunities," in *2nd Summit on Advances in Programming Languages*. Schloss Dagstuhl-Leibniz-Zentrum fuer Informatik, 2017.
[26] S. Ahmed, N. A. Bhatti, M. H. Alizai, J. H. Siddiqui, and L. Mottola, "Efficient intermittent computing with differential checkpointing," in *Proceedings of the 20th ACM SIGPLAN/SIGBED International Conference on Languages, Compilers,*

and Tools for Embedded Systems, 2019.
[27] V. Liu, A. Parks, V. Talla, S. Gollakota, D. Wetherall, and J. R. Smith, "Ambient backscatter: Wireless communication out of thin air," *ACM SIGCOMM Computer Communication Review*, vol. 43, no. 4, pp. 39–50, 2013.
[28] S. Y. Cheung, "Performance Analysis of the unslotted 1-persistent CSMA protocol," mathcs.emory.edu/~cheung/Courses/558/Syllabus/00/CSMA/csma-anal1a, accessed: 2020-02-18.
[29] G. Casella and R. Berger, *Statistical Inference*, ser. Duxbury advanced series in statistics and decision sciences. Thomson Learning, 2002.
[30] ZF Switch, "TIDA-00690," https://www.ti.com/tool/TIDA-00690, accessed: 2021-10-28.
[31] P. N. et al., "Design Optimization and Implementation for RF Energy Harvesting Circuits," *IEEE Jour. on Emerg. and Sel. Topics in Circuits & Systems*, vol. 2, no. 1, pp. 24–33, 2012.
[32] Texas Instruments, "CC1352R product page," ti.com/product/CC1352R#, accessed: 2019-05-07.
[33] ericsson.com, "Realizing smart manufacturing through IoT," ericsson.com/en/mobility-report/articles/realizing-smart-manufact-iot, [accessed: 2020-06-07].
[34] N. K. et al., "Pushing the Boundaries of IoT: Building and Testing Self-powered Batteryless Switch," in *IEEE WF-IoT*, 2019, pp. 231–236.
[35] V. Mangal and P. R. Kinget, "28.1 A 0.42nW 434MHz -79.1dBm Wake-Up Receiver with a Time-Domain Integrator," in *IEEE ISSCC*, 2019, pp. 438–440.
[36] R. Piyare, A. L. Murphy, C. Kiraly, P. Tosato, and D. Brunelli, "Ultra Low Power Wake-Up Radios: A Hardware and Networking Survey," *IEEE Comm. Sur. and Tut.*, vol. 19, no. 4, pp. 2117–2157, 2017.